Comparisons between POLDER 2 and MODIS/Terra aerosol retrievals over ocean

B. Gérard,[1] J.-L. Deuzé,[1] M. Herman,[1] Y. J. Kaufman,[2] P. Lallart,[1] C. Oudard,[1] L. A. Remer,[2] B. Roger,[3] B. Six,[4] and D. Tanré[1]

[1] This paper presents a comparison between simultaneous radiance measurements and aerosol retrievals of POLDER 2/ADEOS 2 and MODIS/Terra, two instruments devoted to monitor the Earth and its atmosphere from space. This study focuses on aerosol remote sensing over ocean. Geophysical results from both inversions are compared. MODIS and POLDER total radiance (and also polarized radiance for POLDER) measurements are compared with radiance simulations based on POLDER and MODIS inversed aerosol products (cross-simulations). Such comparisons emphasize advantages of each instrument and its inversion process. Both instruments generally agree on aerosol retrievals except when POLDER detects nonspherical particles within the coarse mode, which is not possible for MODIS. Combining measurements provided by POLDER 2 and MODIS, the spectral variation of optical properties of nonspherical aerosols can be derived. In order to retrieve more accurately aerosol optical properties, combining directional and polarized information from POLDER 2 with simultaneous MODIS spectral data is needed. The results of this study will guide us in the realization of a coupled inversion scheme.

1. Introduction

[2] Although they are minor constituents of the atmosphere, aerosols are known to be major actors in the climate system and the hydrologic cycle [*Ramanathan et al.*, 2001; *Kaufman et al.*, 2002]. However, large uncertainties in the quantification of their effects remain. Indeed, there is a large variability in aerosol shape, size, optical and chemical properties, and moreover, the short lifetime of these particles and their various origins lead to a highly inhomogeneous distribution within the atmosphere. Ground-based Sun photometers within the AERONET network are well suited to observe continuously the atmosphere in key locations but not on a global scale [*Dubovik et al.*, 2002a]. Only satellite observations can provide daily and global measurements. A large panel of instruments devoted to monitoring aerosols has been successfully launched such as POLDER [*Deschamps et al.*, 1994] on board ADEOS spacecrafts or MODIS [*Salomonson et al.*, 1989] on Aqua or Terra spacecrafts as well as MISR on Terra [*Diner et al.*, 1998]. POLDER 1 and 2 are not acquiring data anymore because of solar panel failure, but they are being replaced by a similar instrument, PARASOL. These new capabilities have already improved our knowledge of aerosol properties [*Kaufman et al.*, 1997; *Mishchenko and Travis*, 1997; *Tanré et al.*, 1997; *Martonchik et al.*, 1998; *Deuzé et al.*, 2000; *Deuzé et al.*, 2001]. Nevertheless, each instrument has its own characteristics leading to different ways of retrieving aerosol properties and to different accuracies in these retrievals. From this point of view, a first step consisting of an intercomparison between results from several sensors, like in the work of *Myhre et al.* [2004], provides interesting information. In a second step, actually using simultaneous information about aerosols provided by different instruments is particularly attractive. The A-train experiment, which consists of several satellites following each other very closely on near orbits, gives us this opportunity.

[3] PARASOL and MODIS on Aqua are parts of the A-Train constellation of satellites. They are both devoted to atmospheric monitoring by measuring the solar radiation reflected by the Earth-atmosphere system but using different techniques. PARASOL performs directional and polarized measurements in nine spectral channels (from 443 to 1020 nm), whereas MODIS measures radiances in only one direction and with no information on polarization but in more spectral channels (from 415 nm to 14.235 μm). Another advantage of MODIS is its pixel size at nadir: from 250×250 m^2 to 1×1 km^2, depending on channel,

---

[1] Laboratoire d'Optique Atmosphérique, Université des Sciences et Technologies de Lille, Villeneuve d'Ascq, France.
[2] Laboratory for Atmospheres, NASA Goddard Space Flight Center, Greenbelt, Maryland, USA.
[3] Pôle ICARE, Université des Sciences et Technologies de Lille, Villeneuve d'Ascq, France.
[4] Centre de Ressources Informatiques, Université des Sciences et Technologies de Lille, Villeneuve d'Ascq, France.

when PARASOL has a spatial resolution of 6×6 km^2. This better resolution combined with capability to perform thermal measurements results in a higher sensitivity to the presence of clouds for MODIS compared to PARASOL. The two sensors clearly have different advantages, which are somehow complementary, so combining PARASOL directional and polarized information with MODIS near and middle-infrared measurements should be particularly interesting. Since PARASOL has been launched in December 2004, data are not yet available but POLDER 2, which performed measurements from April 2003 to October 2003, can be used to do such a study in combination with the MODIS instrument on board the Terra platform.

[4] This study focuses on aerosol monitoring over ocean; a short description of POLDER and MODIS instruments and data are presented in section 2, as well as related aerosol algorithms in section 3. We have proceeded to a pixel by pixel comparison of measurements and geophysical values obtained from each instrument: the way to link POLDER 2 and MODIS near pixels in time and in space (i.e., coincidences) is described in section 4. Comparisons of the resulting geophysical parameters are reported in section 5. In section 6, cross-simulations of measurements are provided; for example, they consist in comparing MODIS measured radiances with radiance simulations based on POLDER aerosol products and on MODIS viewing characteristics (geometry and wavelengths). In section 7, we focus on nonspherical particles and present a method for getting information on the nonspherical model used by POLDER in the middle-infrared.

2. Description of the Sensors

2.1. POLDER Instrument and Data

[5] The POLDER instrument consists of a charged coupled device matrix array detector, a rotating filter wheel, and wide field of view optics, for both along-track and cross-track directions, allowing a near-complete daily coverage of the Earth surface [*Deschamps et al.*, 1994]. It can observe a terrestrial target from different viewing angles, up to 14 directions. POLDER can make use of nine spectral channels (from 443 to 910 nm) and three of them are equipped with analyzers in order to realize polarization measurements: 443, 670, and 865 nm. The two last bands are particularly interesting for aerosol studies over the ocean. Indeed, the aerosol signal at these wavelengths is almost uncontaminated by molecular scattering and water leaving radiance is equal or near zero and quite constant over open ocean. The pixel size is 6×6 km^2 at nadir. The data are normalized radiance

$$R_\lambda = \frac{\pi R_\lambda^*}{E_{s\lambda}},$$

where R_λ^* is the measured radiance at the top of the atmosphere and $E_{s\lambda}$ is the solar irradiance in the considered channel. In the polarized channels, the measurements through three analyzers with different directions (60° apart) allow to retrieve both the normalized total radiance, R_λ, and the normalized polarized radiance, Rp_λ (or, equivalently, the normalized Stokes parameters Q_λ and U_λ associated to the linearly polarized light).

[6] For aerosol studies, cloud-free pixels are selected; then the measurements are corrected for gaseous absorption and stratospheric aerosol contribution. The data which are used as inputs of the algorithm consist of total and polarized radiances averaged over the clear pixels within a 3×3 grid of pixels (i.e., a super-pixel $\approx 20 \times 20$ km^2).

2.2. MODIS Instrument and Data

[7] MODIS is a wide field of view imager [*Salomonson et al.*, 1989; *King et al.*, 1992] that performs acquisitions in 36 spectral channels ranging from 415 nm to 14,235 nm. Compared to POLDER, there is only one viewing direction for a given pixel and no polarization measurements are performed. MODIS pixel resolution at nadir is 250 m, 500 m, or 1 km, depending on spectral channel. For aerosol studies over the ocean, six wavelengths are used: 553, 644, 855, 1243, 1632, and 2119 nm. The 644 and 855 nm channels are 250 m resolution while the other wavelengths are 500 m resolution, which leads to a necessary averaging of the measurements acquired at 250 m resolution channels to 500 m resolution. Like POLDER 2, the measurements are corrected for gaseous absorption and possible stratospheric aerosols contribution. The algorithm is applied on a super-pixel scale which corresponds to 20×20 pixels at 500 m resolution (10×10 km^2). Cloud screening [*Remer et al.*, 2005] is applied to each of the 400 pixels; then the 25% brightest and 25% darkest cloud-free pixels remaining are discarded. The inputs of the algorithm are the average of the measurements of the remaining pixels. These data are given as normalized reflectances ρ_λ which can be linked to normalized radiances R_λ by

$$\rho_\lambda = \frac{R_\lambda}{\mu_s},$$

where μ_s is the cosine of the Sun zenith angle.

3. Principle of POLDER and MODIS Aerosol Inversions Over Ocean

[8] The POLDER and MODIS aerosol algorithms over ocean aim at deriving aerosol properties (also called aerosol products) from precomputed normalized radiance tables comparisons with POLDER 2 or MODIS measurements as described in the work of *Deuzé et al.* [2000] and *Herman et al.* [2005] for POLDER and in the work of *Tanré et al.* [1997], *Levy et al.* [2003], and *Remer et al.* [2005] for MODIS.

3.1. Description of the Look-Up Tables (LUT)

[9] Aerosol size distribution is assumed to be the sum of two contributions, one coming from small spherical (fine mode) aerosols and the other from large (coarse mode) aerosols. MODIS inversion considers only large spherical particles, whereas POLDER inversion's large particles can be either spherical, nonspherical, or a mixture of both. The size distributions of spherical particles (small or large) are described by a log-normal law $n(r)$ defined by two parameters, namely, the mean radius r_m and the logarithm of the standard deviation σ:

$$n(r) = \frac{N_0}{\sigma \ln(10) r \sqrt{2\pi}} \exp\left\{ -\frac{1}{2} \left[\frac{\log r - \log r_m}{\sigma} \right]^2 \right\} \quad (1)$$
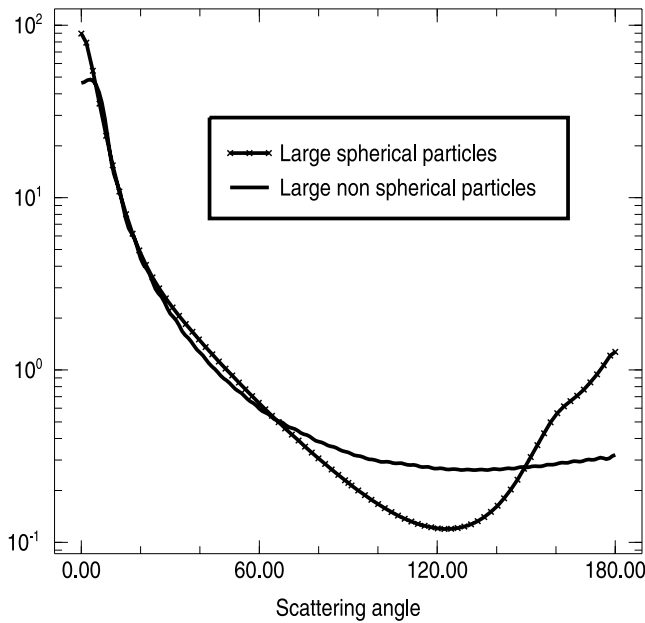
Figure 1. Phase functions of large spherical particles (mode 8 in MODIS LUT, see Table 2) and large nonspherical particles (mode 13-L in POLDER LUT, see Table 1) at 865 nm.

with

$$\int_0^{+\infty} n(r)dr = N_0, \qquad (2)$$

where r is the aerosol radius, N_0 is the total number of particles per unit of volume, and $n(r)dr$ is the number of particles per unit of volume with radius between r and $r + dr$. In addition, for characterizing the spherical aerosol component, we need a refractive index m in order to compute the scattering matrices and extinction coefficients using Mie theory. POLDER inversion is considering aerosol models with refractive indices spectrally independent and with no imaginary part, which means that the POLDER inversion assumes nonabsorbing aerosols. On the other

hand, refractive indices of aerosol models from MODIS inversion are wavelength-dependent, fixed for each mode, and exhibit an imaginary part.

[10] Large nonspherical aerosols can hardly be described in a theoretical way, so an experimental model [*Volten et al.*, 2001] has been implemented in the POLDER LUT. It has been obtained in the visible part of the electromagnetic spectrum from the averaging of measured scattering matrices of different representative aerosol samples. The resulting phase function is compared to one holding for large spherical particles in Figure 1. We assume the nonspherical model to be spectrally independent in terms of extinction cross section and phase matrix in the POLDER LUT and also to be nonabsorbing. The fraction of nonspherical particles (at 865 nm) within the coarse aerosols is noted p.

[11] The POLDER LUT consists of 12 fine modes and 13 coarse modes, defined by the parameters reported in Table 1. The MODIS models properties (4 fine and 5 coarse modes) are derived from AERONET data and LANDSAT Thematic Mapper image analysis [*Levy et al.*, 2003] and are reported in Table 2.

[12] The POLDER LUT are built with a radiative transfer code based on successive orders of scattering [*Deuzé et al.*, 1988]. The Stokes parameters I_λ, Q_λ, and U_λ are calculated at the top of the atmosphere and computation includes multiple scattering in the atmosphere by molecules and aerosols and takes into account the ocean-atmosphere interaction. This last contribution is composed of the Fresnel reflection on the rough ocean surface (wind speed is fixed to 5 m s^{-1} for this effect) and of the water-leaving reflectance ρ_ω coming from underwater scattering elements ($\rho_\omega = 0.001$ at 670 nm and 0.000 at 865 nm). Reflection from foam depends strongly on the wind strength and therefore is not computed in the LUT but is accounted for by a direct correction on the measurements. The Sun glint corresponds to direct Fresnel reflection on the ocean surface and since the corresponding aerosol signal is much smaller in these conditions, a Sun glint mask is applied to remove measurements performed around the direction of the specular reflection.

[13] The MODIS LUT is computed with *Ahmad and Fraser* [1982] radiative transfer code, for a set of aerosol optical thicknesses and viewing geometries. The wind speed is fixed to 6 m s^{-1} and water-leaving radiance is assumed to be equal to zero except for the 553 nm channel where its

Table 1. Description of Aerosol Modes Used to Compute POLDER Look-Up Tables[a]

Small Modes	r_m, μm	m	Large Modes	m	p %
1-S	0.04	1.35 − 0.0i	1-L	1.33 − 0.0i	0
2-S	0.04	1.45 − 0.0i	2-L	1.35 − 0.0i	0
3-S	0.04	1.60 − 0.0i	3-L	1.37 − 0.0i	0
4-S	0.08	1.35 − 0.0i	4-L	1.33 − 0.0i	25
5-S	0.08	1.45 − 0.0i	5-L	1.35 − 0.0i	25
6-S	0.08	1.60 − 0.0i	6-L	1.37 − 0.0i	25
7-S	0.10	1.35 − 0.0i	7-L	1.33 − 0.0i	50
8-S	0.10	1.45 − 0.0i	8-L	1.35 − 0.0i	50
9-S	0.10	1.60 − 0.0i	9-L	1.37 − 0.0i	50
10-S	0.13	1.35 − 0.0i	10-L	1.33 − 0.0i	75
11-S	0.13	1.45 − 0.0i	11-L	1.35 − 0.0i	75
12-S	0.13	1.60 − 0.0i	12-L	1.37 − 0.0i	75
			13-L	-	100

[a]Significance of each term is given in section 3.1. For small modes, σ = 0.2. For large spherical modes, r_m = 1 μm and σ = 0.3. Note that r_m, σ and m are only given to characterize the spherical particles and do not concern the large nonspherical mode.

Table 2. Description of Aerosol Modes Used to Compute MODIS Look-Up Tables[a]

r_m, μm	σ	m (466 to 865 nm)	m (1243 nm)	m (1632 nm)	m (2119 nm)
		Small Modes			
1 0.07	0.17	1.45 − 0.0035i	1.45 − 0.0035i	1.43 − 0.01i	1.40 − 0.005i
2 0.06	0.26	1.45 − 0.0035i	1.45 − 0.0035i	1.43 − 0.01i	1.40 − 0.005i
3 0.08	0.26	1.40 − 0.002i	1.40 − 0.002i	1.39 − 0.005i	1.36 − 0.003i
4 0.1	0.26	1.40 − 0.002i	1.40 − 0.002i	1.39 − 0.005i	1.36 − 0.003i
		Large Modes			
5 0.4	0.26	1.45 − 0.0035i	1.45 − 0.0035i	1.43 − 0.0035i	1.43 − 0.0035i
6 0.6	0.26	1.45 − 0.0035i	1.45 − 0.0035i	1.43 − 0.0035i	1.43 − 0.0035i
7 0.8	0.26	1.45 − 0.0035i	1.45 − 0.0035i	1.43 − 0.0035i	1.43 − 0.0035i
8 0.6	0.26	1.53 − 0.001i	1.46 − 0.0i	1.46 − 0.001i	1.46 − 0.0i
9 0.5	0.35	1.53 − 0.001i	1.46 − 0.0i	1.46 − 0.001i	1.46 − 0.0i

[a]Significance of each term is given in section 3.1.

value is fixed to 0.005. Fresnel reflection on the waves is taken into account, as well as the foam reflection. A Sun glint mask is also applied. If MODIS viewing geometry falls within the Sun glint mask, the pixel is simply discarded, whereas, by taking advantage of its several viewing directions, POLDER may remove some of the measurements associated to a pixel but still keep the remaining measurements and use them in the inversion.

[14] Presently, the most significant differences between the POLDER and MODIS LUT are due to nonspherical particles that POLDER can handle [*Herman et al.*, 2005], when the spectral MODIS measurements are not sensitive to the particle shape, as noticed in the work of *Levy et al.* [2003].

3.2. Inversion Processes

[15] As shown by *Wang and Gordon* [1994], the radiance at the top of the atmosphere due to a mixing of two modes can be approximated by

$$R_\lambda^T(\theta_s, \theta_v, \Phi, \delta_\lambda^T) = c_\lambda \cdot R_\lambda^S(\theta_s, \theta_v, \Phi, \delta_\lambda^T) + (1 - c_\lambda)$$
$$.R_\lambda^L(\theta_s, \theta_v, \Phi, \delta_\lambda^T) \qquad (3)$$

with

$$c_\lambda = \frac{\delta_\lambda^S}{\delta_\lambda^T} \qquad (4)$$

where R_λ^T, R_λ^S, and R_λ^L are the total, small mode, and large mode radiances, respectively (computed with the same total aerosol optical thickness δ_λ^T), θ_s is the solar zenith angle, θ_v is the viewing zenith angle, and Φ is the relative azimuth angle. Here δ_λ^S and δ_λ^L are the small and large mode aerosol optical thicknesses, respectively ($\delta_\lambda^T = \delta_\lambda^S + \delta_\lambda^L$). All the optical parameters are wavelength dependent.

[16] The POLDER inversion is divided into two steps. The first step consists of computing δ_λ^T and c_λ for each pair of modes (12 fine modes × 13 coarse modes, which leads to 156 possible pairs) in order to match the averaged measured radiances at 670 and 865 nm. Some pairs may be unable to lead to a solution and they are eliminated for the rest of the inversion. At that point, if level of signal or range of scattering angles covered by the measurements are too low or too small, respectively, one or several parameters of the fine and coarse modes may be fixed by the algorithm, thus reducing the number of pairs. Then, in the second part of the inversion process, directional total and polarized radiance simulations are computed for each pair with the values of aerosol optical thickness and small mode fraction found in the first step and for all the geometries of the measurements. Quadratic absolute errors in the restitution of total and polarized measurements, ΔR and ΔRp, respectively, can be thus computed.

$$\Delta R_\lambda = \sqrt{\frac{1}{N}\sum_{i=1}^{N}\left[R_\lambda^{meas}(\Theta_i) - R_\lambda^{comp}(\Theta_i)\right]^2} \qquad (5)$$

$$\Delta Rp_\lambda = \sqrt{\frac{1}{N}\sum_{i=1}^{N}\left[Rp_\lambda^{meas}(\Theta_i) - Rp_\lambda^{comp}(\Theta_i)\right]^2}, \qquad (6)$$

where R_λ^{meas} and R_λ^{comp} are the measured and computed total radiances, Rp_λ^{meas} and Rp_λ^{comp} are the measured and computed polarized radiances obtained from Q_λ and U_λ Stokes parameters, N is the number of POLDER 2 viewing directions remaining after the Sun glint mask. Θ_i is the scattering angle and λ can be either 670 or 865 nm. The pair of modes for which the total error is minimal is the POLDER solution. Thus the products given by the inversion are the fine and large modes chosen, δ_{865}^T and c_{865}.

[17] The MODIS inversion scheme is similar. The first step consists of computing δ_{865}^T and c_{865} for each pair of modes (4 fine modes × 5 coarse modes, which leads to 20 possible pairs) in order to minimize the difference ε between measurements and computations in the different spectral channels. In the second step, the pair with the smallest difference is kept as the best one. Here ε is defined in equation (7).

$$\varepsilon = \sqrt{\frac{1}{6}\sum_{k=1}^{6}\left[\frac{R_k^{meas} - R_k^{comp}}{R_k^{meas} + 0.01}\right]^2}, \qquad (7)$$

where k is the spectral channel index and R_k^{meas} and R_k^{comp} are the measured and computed radiances. The outputs of the algorithm are the fine and coarse modes found as the best pair and the associated total, small, and large mode aerosol optical thicknesses at all MODIS aerosol wavelengths.

[18] Both inversions allow us to determine important parameters like aerosol optical thickness and small and large modes fractions as well as their spectral variation, which permits us to compute Angström exponent α defined by

$$\frac{\delta_{670}^T}{\delta_{865}^T} = \left(\frac{670}{865}\right)^{-\alpha}.$$

4. POLDER 2–MODIS/Terra Coincidences

[19] The comparison between the two aerosol retrievals is done at super-pixel scale, 20×20 km² for POLDER 2 and 10×10 km² for MODIS. The comparison is performed by matching POLDER 2 and MODIS super-pixels both in time (±5 min) and space, i.e., given a POLDER 2 super-pixel, the selected MODIS super-pixel is the closest to the POLDER 2 super-pixel center. In addition, only super-pixels that are fully cloud-free at the individual pixel scale, according to the cloud screening provided by both instruments, are considered.

[20] Regarding temporal coincidence, both platforms must have very close ascending (or descending) node local passing time, which is the case for ADEOS 2 and EOS Terra (10:30 a.m., descending node) but not the case for EOS Aqua which passes at 1:30 p.m. (ascending node). We then select EOS Terra and ADEOS 2 orbits with node passing UTC time ±5 min apart. This occurs for about 10 days per month and, for each day, four orbits are concerned. Therefore we have available about 40 coincident orbits per month. Once the temporal selection is made, we have good spatial coverage (same geographical area) between
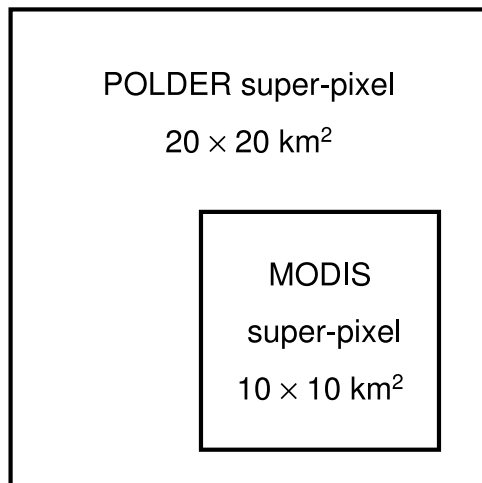
Figure 2. Illustration of a coincidence: a MODIS super-pixel is associated to a POLDER super-pixel.

POLDER 2 and MODIS Terra selected orbits, but we still need to map individual pixels in order to associate every POLDER 2 elementary pixel (6×6 km^2 size) with all MODIS elementary pixels at 1×1 km^2 size included in it. Coincidence tables allows us to determine which MODIS pixel is the nearest to the center of one POLDER 2 pixel, and hence, as shown on Figure 2, which MODIS super-pixel (10×10 km^2) is the nearest to the center of one POLDER 2 super-pixel (20×20 km^2).

5. Comparisons of Inversion Results

[21] Thirty coincident orbits have been selected (corresponding to about 40,000 coincidences between POLDER and MODIS pixels). They cover the 6 months of POLDER 2 data acquisition, from May to October 2003, and are representative of typical geographic zones. The first step in the comparison is to compare results of both inversions, i.e., aerosol optical thicknesses at 865 nm, Angström exponents and small mode fractions at 865 nm.

5.1. Comparison of Aerosol Optical Thickness

[22] We first compare the aerosol optical thicknesses at 865 nm derived from POLDER and MODIS for all the 30 selected coincident orbits with respect to particle size and aerosol type. Practically, we selected cases where POLDER retrievals indicate the presence of mainly small spherical (case 1), large spherical (case 2), or large nonspherical particles (case 3). The corresponding criteria are given in Table 3. Of course, classification resulting from the MODIS retrievals can be different especially in presence of non-spherical particles.

[23] Comparisons are reported in Figure 3a, for all coincidences, and in Figures 3b, 3c, and 3d for cases 1, 2, and 3, respectively. Linear fits are applied in each plot and results are presented in Table 4. Average values of POLDER and MODIS aerosol optical thicknesses at 865 nm and average of the difference between them are also reported in Table 4. The slope of the linear fit applied in Figure 3a is 0.69 which means that MODIS is, in average, underestimating the aerosol optical thickness, compared to POLDER, by

about 30%. However, the bias is not systematic and depends on particle sizes, as noted in Figures 3b, 3c, and 3d. For case 1, the slope of the linear fit is 0.97 with a very good correlation coefficient (0.98) which means the aerosol optical thicknesses derived by the two sensors in the accumulation mode are very consistent. The average difference between aerosol optical thicknesses for case 1 is only of 0.023. For case 2, the slope is 0.77 with a lower correlation coefficient (0.84). Although case 2 of Table 3 allows the presence of nonspherical particles, POLDER results show that large aerosols are mostly spherical. Since case 2 corresponds to maritime aerosols and can be related to a low level of aerosol optical thickness, less than 0.15 for most of the points, Figure 3c shows a relatively correct agreement between the two retrievals, which is not confirmed by the slope of the linear fit but by the average difference between aerosol optical thicknesses of 0.016. As there is no information for this case for high values of aerosol optical thickness, the slope is not significant. Case 3 linear fit gives a slope of 0.60 and a correlation coefficient of 0.95. This case corresponds to a majority of large nonspherical particles and exhibits the lowest agreement between POLDER and MODIS aerosol optical thicknesses. The average difference between aerosol optical thicknesses is the highest of the three cases: 0.071. The explanation is that MODIS considers only spherical aerosols and that there can be large differences between spherical and nonspherical particles properties, as shown on Figure 1 for phase functions.

[24] Presently, the main disagreement between POLDER and MODIS aerosol optical thicknesses results from the presence of nonspherical particles that are determined by POLDER but not by MODIS. When POLDER is retrieving a majority of spherical aerosols, there is a general agreement between the two instruments, especially for small particles.

5.2. Comparison of Size Retrieval

[25] This section deals with comparisons of size retrieval expressed as the Angström exponent (defined using the 670 and 865 nm wavelengths) and the fine mode fraction at 865 nm. Instead of using scatterplots that are difficult to interpret for these parameters, we sort the comparisons according to the absolute value of the difference between POLDER (used as the reference value) and MODIS retrievals. Figures 4a and 4b present, for all coincidences, differences between POLDER and MODIS Angström exponents $|\alpha_{POLDER} - \alpha_{MODIS}|$ and small mode fractions at 865 nm $|c_{POLDER} - c_{MODIS}|$ as a function of α_{POLDER} and c_{POLDER}, respectively. The color scale of Figures 4a and 4b indicates the agreement between POLDER and MODIS retrievals. For these two figures, only coincidences where POLDER aerosol optical thickness at 865 nm is greater than 0.2 have been selected.

Table 3. POLDER Selection Criteria Used to Distinguish Between Several Shapes and Sizes of Aerosols[a]

Case	Majority Presence	% Small	% Large Spherical	% Large Nonspherical
1	Small spherical	70 to 100%	0 to 30%	0 to 30%
2	Large spherical	0 to 30%	70 to 100%	0 to 30%
3	Large nonspherical	0 to 30%	0 to 30%	70 to 100%

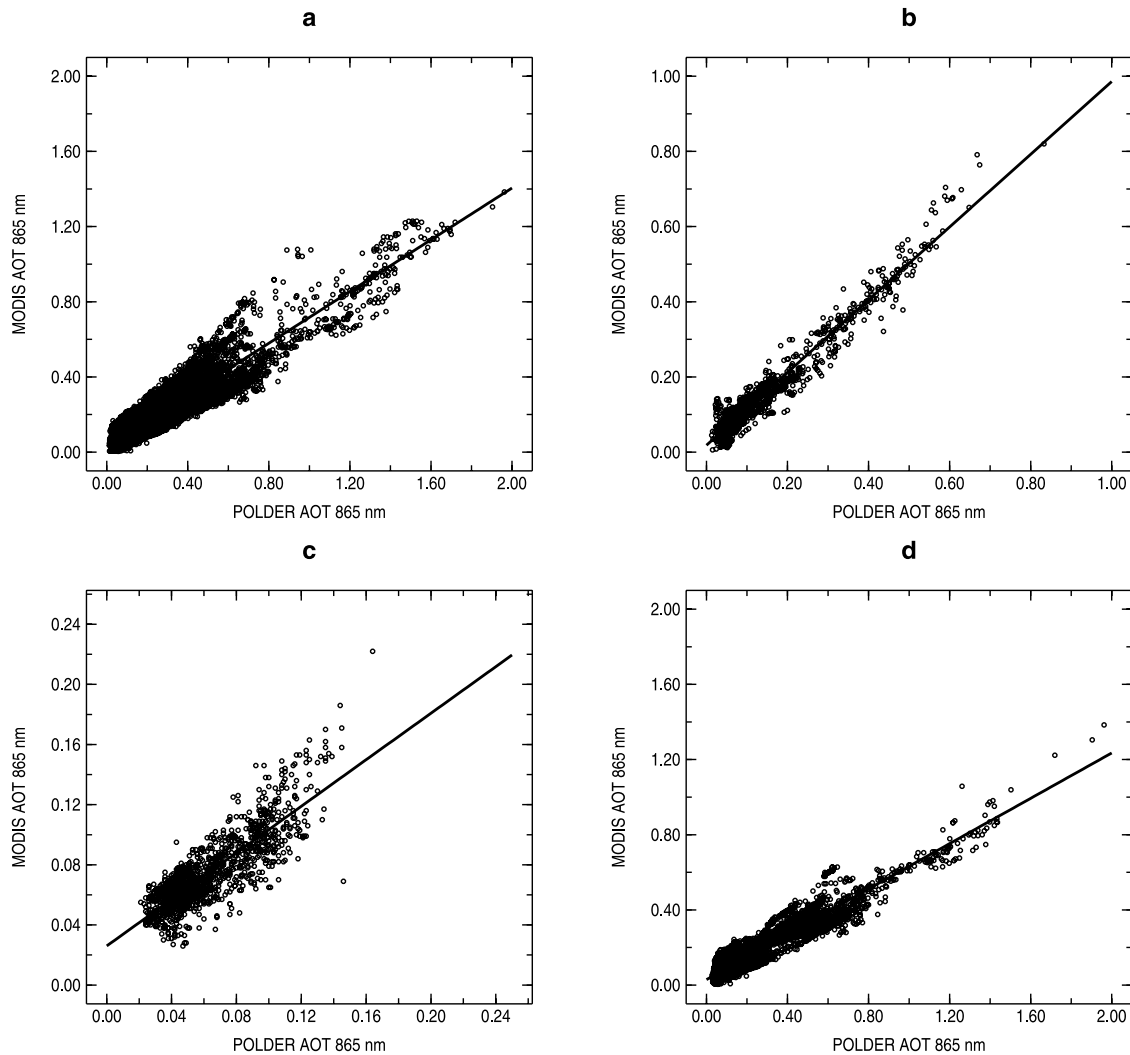[a]The indicated percentages are given at 865 nm.

Figure 3. Aerosol optical thicknesses at 865 nm from POLDER (X-axis) and MODIS (Y-axis) inversions for data of 30 selected coincident orbits. The linear fits are also represented and the corresponding parameters are given in Table 4. In Figure 3a, no selection criterion is applied. In Figures 3b, 3c, and 3d, selection criteria are applied. They correspond to cases 1, 2, and 3 criteria of Table 3, respectively.

Moreover, values of POLDER Angström exponent or aerosol optical thickness corresponding to a small number of coincidences (less than 50) have been rejected.

[26] Average values of POLDER and MODIS Angström exponents and small mode fractions at 865 nm, as well as the average of their absolute differences, for all coincidences, but also for cases 1, 2, and 3 of Table 3, are presented in Table 5. Concerning the average difference between POLDER and MODIS small mode fractions at 865 nm,

the best agreement stands for large spherical particles (13.0%) and the lowest agreement stands for large non-spherical particles (25.3%), which illustrates the importance of aerosols shape. However, POLDER and MODIS algorithms do not use the same set of aerosol models, and thus small mode fractions may not reflect completely the size differences between POLDER and MODIS retrievals. Average difference of Angström exponents between POLDER and MODIS may also be significant but have to be looked at

Table 4. Parameters of the Linear Fits Applied to Plots Presented in Figures 3a, 3b, 3c, and 3d, and Averages of POLDER and MODIS Aerosol Optical Thicknesses at 865 nm ($\overline{\delta_{POLDER}^{865}}$ and $\overline{\delta_{MODIS}^{865}}$, Respectively) and of Their Absolute Difference

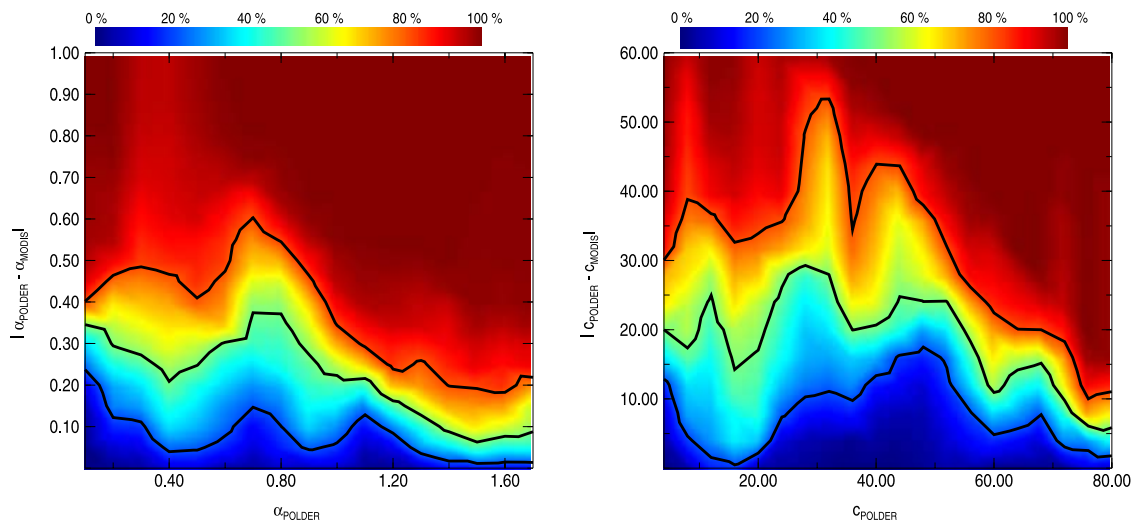| Figure	Slope of the Linear Fit	Offset of the Linear Fit	Correlation Coefficient	$\overline{\delta_{POLDER}^{865}}$	$\overline{\delta_{MODIS}^{865}}$	$\overline{\left|\delta_{POLDER}^{865} - \delta_{MODIS}^{865}\right|}$
3a	0.688	0.029	0.931	0.181	0.155	0.040
3b	0.968	0.018	0.975	0.124	0.138	0.023
3c	0.774	0.026	0.838	0.061	0.074	0.016
3d	0.603	0.029	0.953	0.266	0.205	0.071

Figure 4. Comparison between POLDER and MODIS Angström exponents (Figure 4a, left) and small mode fractions at 865 nm (Figure 4b, right). For a given value of POLDER Angström exponent (read on X-axis), the color scale indicates the percentage of coincidences which satisfy an absolute difference between POLDER and MODIS Angström exponents less than a value chosen on Y-axis. The black lines are associated to color contours corresponding to values 20, 50, and 80% (from bottom to top of the plot, respectively). For example, the point α_{POLDER} = 0.8 and $|\alpha_{POLDER} - \alpha_{MODIS}|$ = 0.1 is located on the first black line, which means that 20% of coincidences where α_{POLDER} = 0.8 have a difference between Angström exponents $|\alpha_{POLDER} - \alpha_{MODIS}|$ less than 0.1. For a given value of POLDER small mode fraction (read on X-axis), the color scale indicates the percentage of coincidences which satisfy an absolute difference between POLDER and MODIS small mode fraction less than a value chosen on Y-axis. The black lines are associated to color contours corresponding to values 20, 50, and 80% (from bottom to top of the plot, respectively). For example, the point c_{POLDER} = 60% and $|c_{POLDER} - c_{MODIS}|$ = 5% is located on the first black line, which means that 20% of coincidences where c_{POLDER} = 60% have a difference between small mode fractions $|c_{POLDER} - c_{MODIS}|$ less than 5%.

carefully. Indeed, the lowest agreement stands for small particles (average difference of 0.524) but it has to be compared to POLDER average Angström exponent for this case (1.981). The relative difference is then about 25%, whereas this relative difference reaches about 90% for large spherical particles and about 180% for large nonspherical particles. This illustrates again the importance of particle shape but also the impact of the set of aerosol models used, which also plays a role in the inversion.

[27] On Figure 4a and 4b, the best agreement is observed for α_{POLDER} > 1.2 (see Figure 4a) and c_{POLDER} > 60% (see Figure 4b), which indicates predominance of small particles. For greater α_{POLDER}, the comparison is not reported because of too small number of coincidences. For lower values of α_{POLDER} and c_{POLDER}, the agreement is less good but still correct, although the comparison exhibits some local important differences, especially for Angström exponent α_{POLDER} about 0.7 and small mode fraction c_{POLDER}

between 30% and 50%. These values correspond to large particles mixed with a nonnegligible part of small particles. Among large particles, POLDER distinguishes spherical or nonspherical aerosols, whereas MODIS can handle only spherical particles. Statistically, intermediate values of POLDER Angström exponent and small mode fraction presented above often correspond to small particles associated with nonspherical ones and only rarely to a mixing of small and large spherical particles. Thus the highest differences between POLDER and MODIS retrievals result from differences in the shape of large particles.

[28] To summarize, POLDER and MODIS inversions globally give comparable fine mode fractions and Angström exponents, although some differences cannot be ignored. The shape of larger particles is an issue but the role of particle shape has to be confirmed and estimated. A better determination of Angström exponent or small mode fractions will need to combine POLDER and

Table 5. Average of POLDER and MODIS Angström Exponents ($\overline{\alpha_{POLDER}}$ and $\overline{\alpha_{MODIS}}$) and Small Mode Fractions at 865 nm ($\overline{c_{POLDER}}$ and $\overline{c_{MODIS}}$) and of Their Absolute Differences

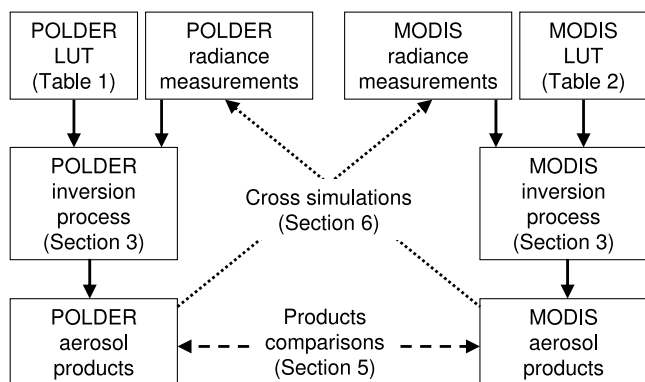| Case	$\overline{\alpha_{POLDER}}$	$\overline{\alpha_{MODIS}}$	$\overline{|\alpha_{POLDER} - \alpha_{MODIS}|}$	$\overline{c_{POLDER}}$	$\overline{c_{MODIS}}$	$\overline{|c_{POLDER} - c_{MODIS}|}$
All Coincidences	0.772	0.907	0.327	0.280	0.430	0.219
1 – Small Spherical Particles	1.981	1.508	0.524	0.804	0.660	0.206
2 – Large Spherical Particles	0.327	0.234	0.306	0.143	0.199	0.130
3 – Large Nonspherical Particles	0.216	0.587	0.396	0.068	0.317	0.253

Figure 5. Flowchart of POLDER and MODIS inversion and cross-simulation processes.

MODIS information, which should bring more accuracy in the retrievals.

6. Cross-Simulations of Radiances

[29] To further understand the differences between the aerosol products of the two sensors, we perform a sensitivity study. We test the ability of POLDER aerosol products to simulate radiances in the middle-infrared spectral region, beyond the range of the POLDER instrument, and we test these results with MODIS radiance measurements. Likewise, we use MODIS aerosol products to simulate the angular radiation field and test these results with POLDER total and polarized radiance measurements. The reported radiances have been corrected for the well-known molecular contribution in order to focus on aerosol signal. The 1243 nm MODIS channel is not considered because the measurements at this wavelength are noisy. A flowchart illustrating cross-simulation process is given in Figure 5.
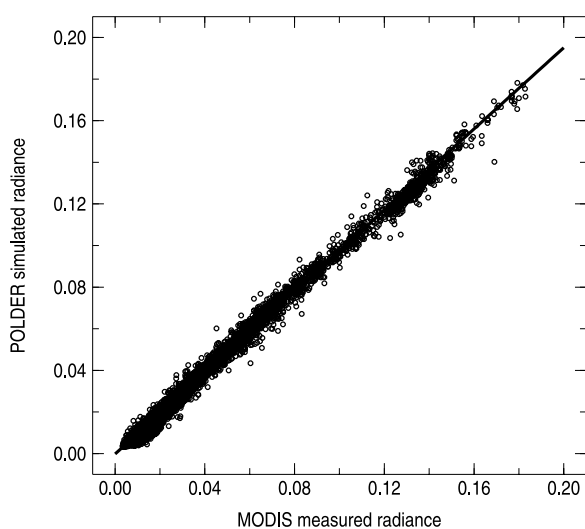

Figure 6. Simulations based on POLDER aerosol products (Y-axis) of MODIS radiance measurements (X-axis) at 855 nm for all coincidences as in Figure 3a. The linear fit is also represented and the corresponding parameters are given in Table 6.

6.1. Simulations of MODIS Radiance Measurements Using POLDER Aerosol Products

[30] Simulations of the total radiances coming from both accumulation and coarse modes are made according to *Wang and Gordon* [1994] approximation (see equation (3)) and by using a radiative transfer code based on successive orders of scattering [*Deuzé et al.*, 1988]. The inputs of the simulations are POLDER aerosol products: aerosol optical thickness at 865 nm, small mode fraction at 865 nm, size distribution and refractive indices of small and large spherical particles and fraction (at 865 nm) of nonspherical aerosols within the coarse mode. The simulations are realized for MODIS viewing geometry and spectral conditions (553, 644, 855, 1632, and 2119 nm wavelengths are considered). Small and large spherical particle contributions have been computed using Mie theory. For nonspherical aerosols, there is no measurement available in the work of *Volten et al.* [2001] that can be used to simulate the radiances in the 1.632 and 2.119 μm MODIS channels. In a first approximation, we assume no spectral variation of the aerosol extinction cross section and of the phase matrix of the nonspherical model. For 553, 644, and 855 nm channels, the assumption is clearly valid as noticed in the work of *Herman et al.* [2005], while in the middle-infrared channels (1632 and 2119 nm), the extrapolation has to be checked. We also assume nonspherical aerosols to be nonabsorbing.

[31] In Figure 6, simulated radiances based on the POLDER aerosol products are plotted against MODIS radiance measurements at 855 nm wavelength for all coincidences. Comparisons for other wavelengths are not shown but linear fits parameters applied on all these plots are presented in Table 6.

[32] In the MODIS wavelengths that are identical or close to POLDER channels, POLDER simulated radiances are quite comparable to MODIS measured radiances (average differences of 3.8% at 553 nm, 0.2% at 644 nm, and 2.4% at 855 nm), whereas large differences are observed in the middle-infrared, where POLDER does not perform any measurements: 14.5% at 1632 nm and 31.7% at 2119 nm. As POLDER 2 and MODIS calibration accuracies are 2 % (from POLDER 2 website) and less than 2%, respectively [*Remer et al.*, 2005], the small differences in the visible and near-infrared can be explained by calibration issues.

[33] In the middle-infrared channels (1632 and 2119 nm), the large differences can result either from the POLDER aerosol model that is not able to correctly estimate the middle-infrared radiances or from assumptions we used for nonspherical particles. Indeed, as previously outlined, to simulate radiances in the middle-infrared channels with

Table 6. Parameters of the Linear Fits Applied in Plot Presented in Figure 6 and on Similar Plots Realized for Other Wavelengths (but Not Shown in This Article)

Wavelength, nm	Slope of the Linear Fit	Offset of the Linear Fit	Correlation Coefficient
553	1.038	−0.004	0.993
644	1.002	0.000	0.996
855	0.976	0.000	0.997
1632	1.145	0.000	0.992
2119	1.317	0.000	0.988

Table 7. Main Results of POLDER and MODIS Inversions for the Three Examples Presented in Figures 7a, 7b, 7c, 9a, 9b, 9c, 10a, 10b, and 10c[a]

	Case a Small Spherical Particles	Case b Large Spherical Particles	Case c Large Nonspherical Particles
	POLDER		
Aerosol optical thickness	0.124	0.100	0.268
Angström exponent	2.039	0.283	0.330
c_{small}	72.9% (4-S)	15.1% (10-S)	6.4 % (3-S)
$c_{large\ spherical}$	37.1% (1-L)	84.9% (2-L)	0.0 % (13-L)
$c_{large\ non-spherical}$	0.0% (1-L)	0.0% (1-L)	93.6% (13-L)
	MODIS		
Aerosol optical thickness	0.149	0.132	0.165
Angström exponent	2.034	0.198	0.730
c_{small}	96.6% (2)	18.6% (4)	21.6% (1)
$c_{large\ spherical}$	3.4% (9)	81.4% (7)	78.4% (6)
$c_{large\ nonspherical}$	-	-	-

[a]Aerosol optical thicknesses and small mode fractions (c_{small}, $c_{large\ spherical}$, and $c_{large\ nonspherical}$) are given at 865 nm. In addition to fine mode fractions, we also report, in parenthesis, the small and large mode numbers retrieved by POLDER (see Table 1) and MODIS (see Table 2) inversions.

POLDER aerosol products, we assume no spectral variation of the nonspherical particles' optical properties, which is doubtful. The slopes of the linear fits depend mainly on points with strong signal (i.e., pixels with the higher radiances) and at 1632 and 2119 nm wavelengths, high radiances correspond to dust events, i.e., nonspherical particles (case 3 of Table 3). Therefore we can relate this systematic higher average error in the middle-infrared with dust particles. One part of these errors may arise from the fact that the POLDER retrieval may not be correct. However, as the errors are systematic, they can only be explained by the presence of nonspherical aerosols that exhibit a spectral variation of their optical properties between visible and middle-infrared.

[34] Three specific cross-simulations, corresponding to examples of cases 1, 2, and 3 of Table 3 (see Table 7), are reported in Figures 7a, 7b, and 7c, respectively. For each case, the three plots correspond to MODIS measured radiances (full dots), and simulated radiances based on POLDER (open squares) or on MODIS (open triangles) aerosol products. For small spherical particles, case 1 of Table 3 (Figure 7a), simulations based on POLDER aerosol products are consistent, although not as accurate as simulations based on MODIS aerosol products. The relative differences in the middle-infrared between MODIS measured radiances and simulated radiances based on POLDER aerosol products are higher on Figures 7b and 7c, which correspond to examples of case 2 (majority of large spherical particles) and case 3 (majority of large nonspherical particles) of Table 3. These two examples show that extrapolation of POLDER aerosol products in the middle-infrared may not simulate precisely MODIS measured radiances when large particles are involved. However, the absolute differences between MODIS measured radiances and simulated radiances based on POLDER aerosol products are higher in Figure 7c (about 0.007 at 2119 nm) than in Figure 7b (about 0.002 at 2119 nm). When large nonspherical particles dominate, the differences are higher and, as previously outlined, systematic: they can not be explained only by errors coming from extrapolation of POLDER aerosol products in the middle-infrared. Spectral behavior of nonspherical aerosol optical properties (that we did not assume in our simulations) is explaining the systematic shift.

[35] In conclusion, simulations of MODIS measured radiances by POLDER aerosol products are correct when large particles are not involved. When the POLDER aerosol products correspond to coarse aerosols, a bias appears in the middle infrared. One part of the bias can be related to inaccurate estimates of the POLDER radiance simulations in the middle-infrared but, when large nonspherical particles are involved, the bias is systematic and due to variation of nonspherical aerosol optical properties between the visible and the middle-infrared.

6.2. Simulations of POLDER Radiance Measurements Using MODIS Aerosol Products

[36] We now check the capability of MODIS aerosol products to correctly simulate the angular behavior of POLDER total and polarized measured radiances. Simulations are based on MODIS aerosol products: total and small mode optical thicknesses at all MODIS aerosol wavelengths as well as size distributions and refractive indices for fine and coarse modes (both spherical). As in section 6.1, total radiances are computed according to *Wang and Gordon* [1994] approximation (see equation (3)) and by using a radiative transfer code based on successive orders of scattering [*Deuzé et al.*, 1988]. The simulations are realized for all POLDER 2 viewing geometries (up to 14) and wavelengths (670 and 865 nm).

[37] Simulated total (Figure 8a) and polarized (Figure 8b) radiances based on the MODIS aerosol products are plotted against POLDER measured radiances at 670 and 865 nm wavelengths for all coincidences. We have plotted the average value of angular measured and simulated radiances. In Figure 8a (total radiances), the slope of the linear fit is 0.987, the offset is 0.000, and the correlation coefficient is 0.989. In Figure 8b (polarized radiances), these values are 0.927, 0.000, and 0.920, respectively. Figures 8a and 8b show that MODIS aerosol products can simulate correctly the averaged angular information, especially for total radiance. We have also computed the following error:

$$\sigma_i = \sqrt{\frac{1}{2N} \sum_\lambda \sum_N \left(\frac{1}{d} \sum_d (R^{meas} - R_i^{simu})^2 \right)},$$

a

b

c
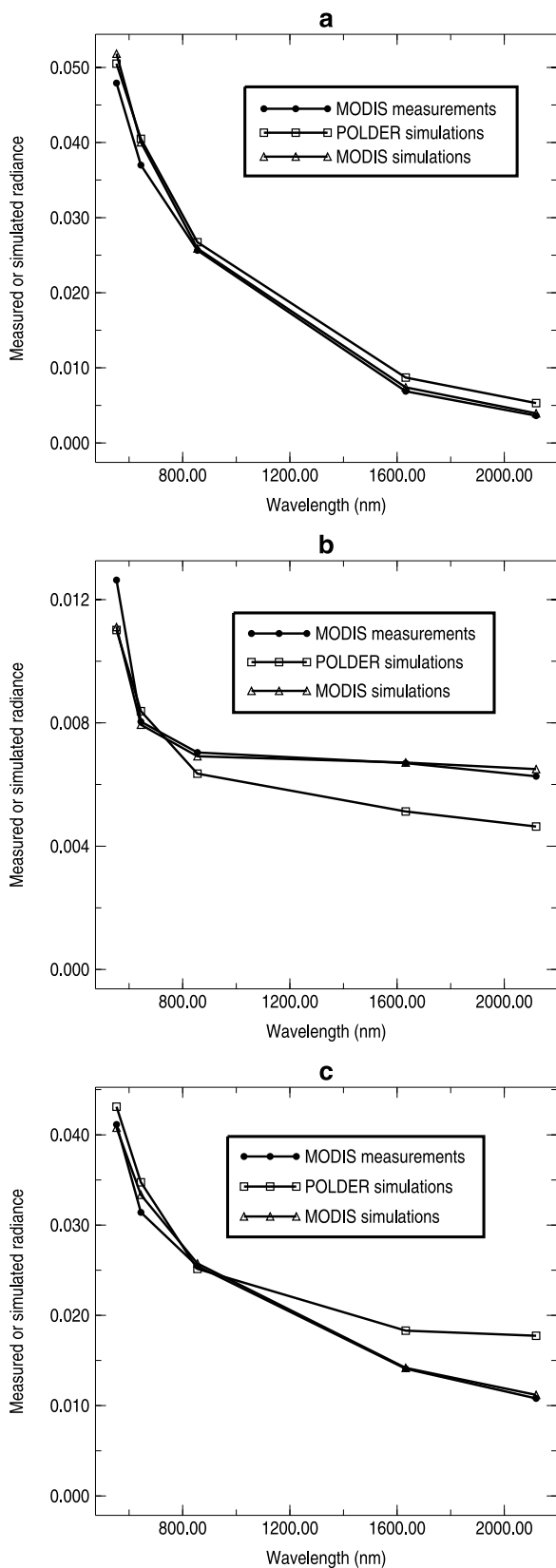
where N is the total number of pixels used in the comparison, d is the number of viewing directions of a given POLDER pixel, R^{meas} is the POLDER measured radiance, and R_i^{simu} is the radiance computed from aerosol products. Here λ is the wavelength, equal to 670 or 865 nm, i is the instrument index: it represents either POLDER or MODIS. We have thus computed errors between POLDER measured and simulated radiances, σ_{POLDER}^{R} and σ_{POLDER}^{PR} (for total and polarized radiance measurements, respectively), and errors between POLDER measured radiances and MODIS simulated radiances, σ_{MODIS}^{R} and σ_{MODIS}^{PR}, both for the whole set of coincidences (all coincidences of Figure 3a) and also for cases described in Table 3. Errors and ratios of POLDER and MODIS errors are presented in Table 8.

[38] For all coincidences, ratio of error between POLDER total radiance measurements and simulations based on POLDER aerosol products and error between POLDER total radiance measurements and simulations based on MODIS aerosol products is 4.33. The ratio is 1.82 if we consider the same errors but for POLDER polarized radiance measurements. If we separate the study according to the shape and size of the particles (cases 1, 2, and 3 of Table 3), the results become very different. For small particles (case 1), the ratios between errors decrease to 2.93 and 1.42, respectively. For large spherical aerosols (case 2), the ratio between errors for total radiances is less than the general case (3.00), but the ratio for polarized measurements is higher (2.36). For nonspherical particles (case 3), both ratios are very high (6.25 and 2.84). These results illustrate the fact that MODIS aerosol products are not able to simulate directional and polarized radiance measurements with an accuracy as high as POLDER aerosol products, especially for case 3, namely nonspherical particles case.

[39] To illustrate our discussion, we plot the POLDER total (Figures 9a, 9b, and 9c) and polarized (Figures 10a, 10b, and 10c) radiance measurements for the three same specific observations as in section 6.1 (see Table 7). For each case, the three plots correspond to POLDER measured radiances (full dots) and to simulated radiances based on POLDER (open squares) or on MODIS (open circles) aerosol products.

[40] Concerning small particles (case 1) example (Figures 9a and 10a), radiance simulations based on MODIS aerosol products are consistent and simulate correctly the trend of POLDER radiance measurements.

[41] Detailed comparison for large spherical particles (case 2) simulations (Figures 9b and 10b) shows that radiance simulations using MODIS aerosol products do not retrieve correctly directionality of POLDER total and polarized radiance measurements and especially the polarization. It can be explained by the real part of the refractive index m_r retrieved by MODIS inversion (and thus given as

---

Figure 7. Simulations, for three given coincidences, of MODIS radiance measurements by POLDER and MODIS aerosol products. Figure 7a corresponds to an example of small spherical aerosols (case 1 of Table 3), Figure 7b to large spherical aerosols (case 2 of Table 3) and Figure 7c to large nonspherical particles (case 3 of Table 3). For these three coincidences, we give main POLDER and MODIS inversion results in Table 7.
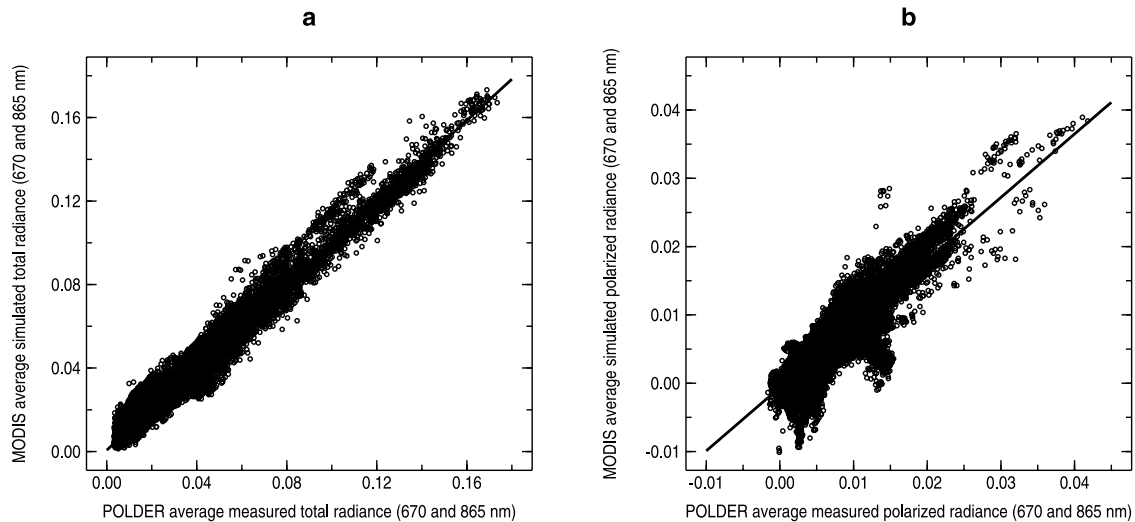
a

b

Figure 8. Radiance simulations based on MODIS aerosol products (Y-axis) of POLDER average total (a) and polarized (b) radiance measurements (X-axis) at 670 and 865 nm for all coincidences as in Figure 3a. The linear fits are also represented and the corresponding parameters are given in section 6.2.

MODIS product) for the coarse mode: 1.45 (at 855 nm), while simulations based on POLDER aerosol products retrieve correctly the polarized data with $m_r = 1.35$. More generally, the comparison of refractive index retrieved by POLDER and MODIS is difficult. The refractive index of nonspherical particles is not precisely known and, for large particles, the ranges of real part of the refractive index covered by POLDER and MODIS aerosol models do not overlap (see Tables 1 and 2).

[42] The highest error ratios (according to Table 8) correspond to large nonspherical particles (case 3) simulations (Figures 9c and 10c) where radiance simulations based on MODIS aerosol products cannot reproduce correctly the POLDER total or polarized radiance measurements, especially in Figure 9c. Moreover, this last example exhibits the highest differences (among the three examples) between POLDER and MODIS aerosol products (see Table 7).

[43] As a conclusion, these results show the importance of the information included in directional total and polarized radiances, which permits us to better constrain the parameters of aerosol models. Case 3 results also illustrate the high contribution brought by including nonspherical particles in the set of aerosol models.

7. Optical Properties of Nonspherical Particles

[44] From previous sections, we see that nonspherical particles appear to be the main point of disagreement between POLDER and MODIS. A dust event over the Cabo Verde Islands (4 October 2003), corresponding to simultaneous measurements performed by POLDER 2 and MODIS, has been selected for further analysis. This event has not been included in the comparisons of section 5.1. We plot in Figure 11 a comparison of POLDER and MODIS aerosol optical thicknesses at 865 nm for this event. Two branches appear in the plot. The upper branch (slope of the linear fit: 1.170, offset: −0.183, and correlation coefficient: 0.982) corresponds to cases where MODIS indicates a large mode with number 5, 6, or 7 of Table 2. The lower branch (slope: 0.653, offset: 0.026, and correlation coefficient: 0.653) corresponds to MODIS large mode number equal to 8 or 9 of Table 2. MODIS large modes 5, 6, and 7 correspond to wet sea-salt particles and 8 and 9 to dust-like particles [*Levy et al.*, 2003]. On Figures 12a and 12b, we plot maps of POLDER and MODIS aerosol optical thicknesses at 865 nm. These maps display a spatial heterogeneity of MODIS aerosol optical thicknesses (Figure 12b) compared to POLDER (Figure 12a). A Sun photometer, located on the Cabo Verde islands (17°N, 23°W), shows a high average value of aerosol optical thickness (0.9 at 870 nm) and variability throughout the day, making a comparison with satellite retrieval hard to realize. The shift of MODIS aerosol optical thickness from one pixel to its neighbor is linked to a shift of large mode number between sea salt (5, 6, or 7) and dust-like aerosols (8 or 9). MODIS can explain the measured spectral information with the same accuracy with sea salt or dust within the large mode but with different associated fine mode and aerosol optical thickness. This shows the necessity to introduce nonspherical particles in the MODIS retrieval process.

Table 8. Errors Between POLDER Radiance Measurements and Radiance Simulations Based on POLDER or MODIS Aerosol Products[a]

Case	σ^R_{POLDER}	σ^R_{MODIS}	$\sigma^R_{MODIS}/\sigma^R_{POLDER}$	σ^{PR}_{POLDER}	σ^{PR}_{MODIS}	$\sigma^{PR}_{MODIS}/\sigma^{PR}_{POLDER}$
All Coincidences	0.00106	0.00459	4.33	0.00119	0.00216	1.82
1 − Small Spherical Particles	0.00100	0.00293	2.93	0.00120	0.00170	1.42
2 − Large Spherical Particles	0.00077	0.00231	3.00	0.00056	0.00132	2.36
3 − Large Nonspherical Particles	0.00108	0.00675	6.25	0.00098	0.00278	2.84

[a]Total and polarized radiances are considered. The definition of the errors is given in section 6.2.
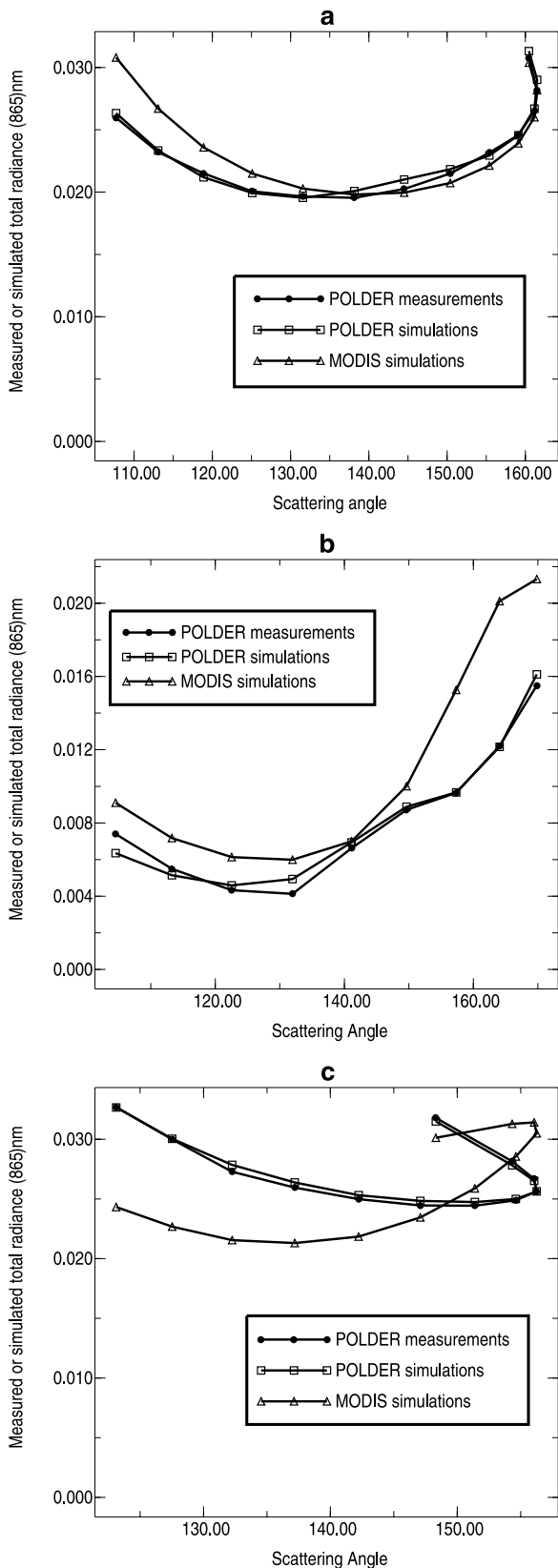
Figure 9. Simulations, for three given coincidences (The same as in Figures 7a, 7b, and 7c, see also Table 7), of POLDER total radiance measurements by POLDER and MODIS aerosol products.
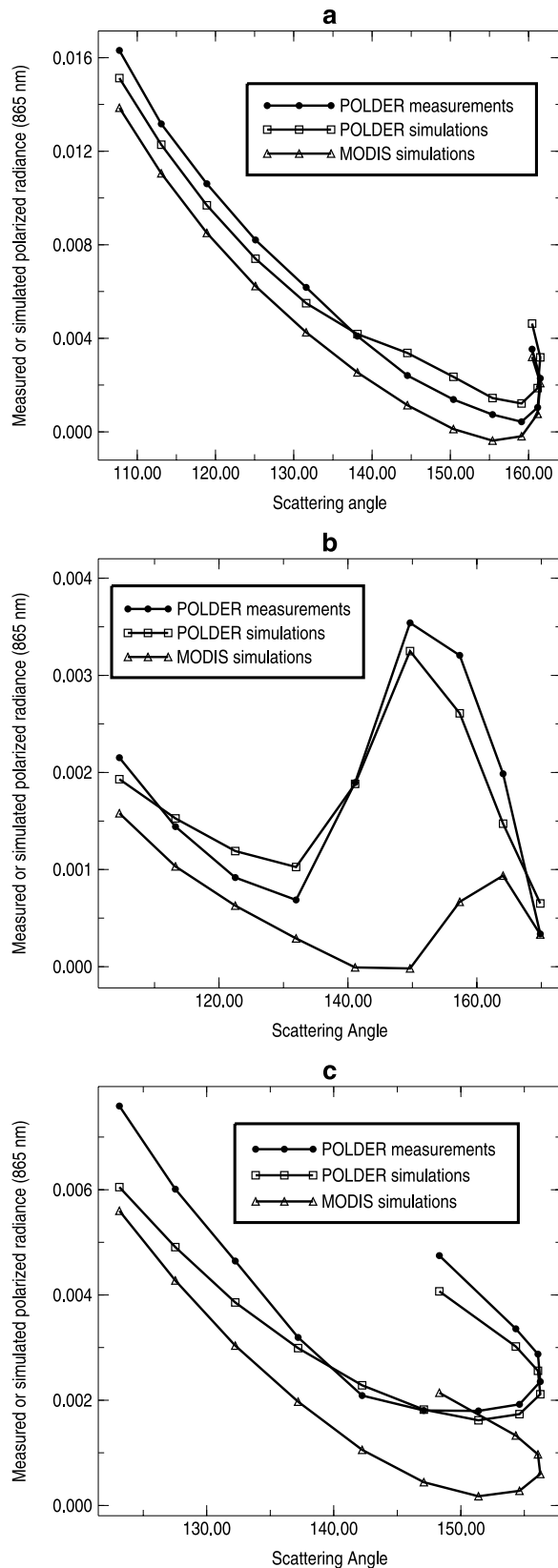

Figure 10. Simulations, for three given coincidences (The same as in Figures 7a, 7b, and 7c, see also Table 7), of POLDER polarized radiance measurements by POLDER and MODIS aerosol products.
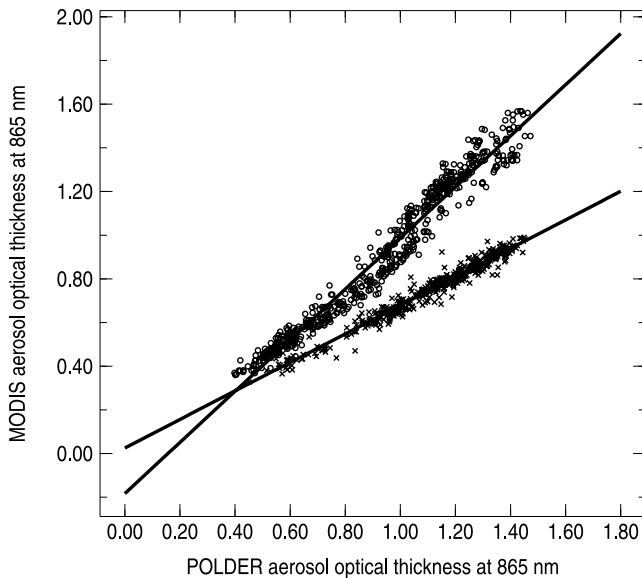
Figure 11. Aerosol optical thicknesses at 865 nm from POLDER (X-axis) and MODIS (Y-axis) inversions for a dust event (4 October 2003) over Cabo Verde area. Open circles correspond to cases where MODIS large mode number is 5, 6, or 7 (wet sea-salt particles), and X signs to MODIS large mode number equal to 8 or 9 (dust-like particles). Linear fit for each branch is also represented. The corresponding parameters are given in section 7.

[45] *Herman et al.* [2005] show that the nonspherical phase matrix of *Volten et al.* [2001] is particularly well adapted to reproduce dust directional properties as measured by POLDER for visible and near-infrared wavelengths. However, optical properties of nonspherical particles present a spectral variation between visible and middle-infrared wavelengths. By assuming that the detection of nonspherical particles by POLDER, at 670 and 865 nm, is correct,

simultaneous MODIS measurements at 1632 and 2119 nm can provide information about the spectral behavior of optical properties of nonspherical particles. To confirm the presence of dust, observations corresponding to nonspherical aerosol optical thicknesses higher than 0.5 and with, at least, seven viewing directions remaining after masking for Sun glint are selected.

[46] According to the *Wang and Gordon* [1994] approximation, the radiance R^{total} due to a mixing of different modes of particles $i = \{$small spherical, large spherical, or large nonspherical particles$\}$ may be written as $R^{total}(\delta) = \sum_i c^i R^i(\delta)$ where $R^i(\delta)$ is the radiance for the mode i computed with total aerosol optical thickness δ and c^i the ratio $\frac{\delta_i}{\delta}$, where δ^i is the aerosol optical thickness of the mode i. The contribution Rad^i of each type i of aerosol is thus $Rad^i = c^i R^i(\delta)$. If we correct MODIS measurements from small and large spherical particles contributions, the remaining radiance represents the nonspherical particles' radiance Rad^{NS}. In the single scattering approximation, this contribution is proportional to the aerosol optical thickness of the nonspherical mode δ^{NS} times the phase function p^{NS} (we suppose here no absorption and thus the single scattering albedo is equal to 1). Assuming the aerosol extinction cross section (and thus optical thickness) is spectrally independent, for any MODIS wavelength λ', we can calculate the nonspherical phase function with

$$p_\lambda^{NS} = p_{\lambda ref}^{NS} \frac{Rad_\lambda^{NS}}{Rad_{\lambda ref}^{NS}},$$

where p_λ^{NS} is the phase function of the nonspherical model at wavelength λ and Rad_λ^{NS} the radiance contribution of the nonspherical model at wavelength λ. $\lambda_{ref} = 644$ nm is the reference wavelength and we derived p_λ^{NS} for $\lambda = 855, 1632,$ and 2119 nm; results are shown in Figure 13.

[47] At 855 nm, the retrieved phase function is close to the phase function at 644 nm. It validates the fact that the POLDER inversion algorithm assumes no change in the
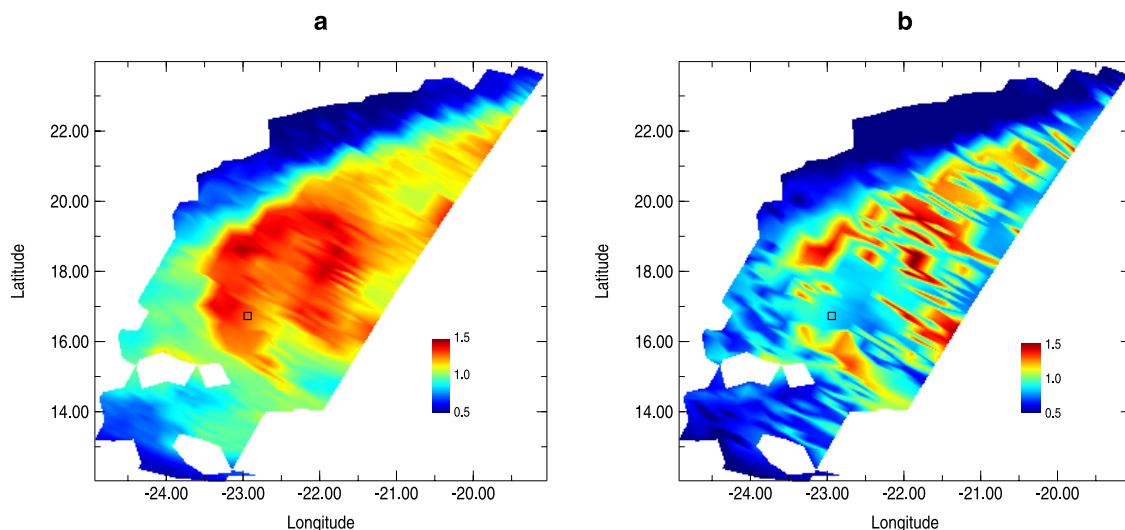

Figure 12. POLDER (a) and MODIS (b) aerosol optical thickness at 865 nm over Cabo Verde area for 4 October 2003. White areas mean no data available. The black square indicates Cabo Verde Sun photometer.
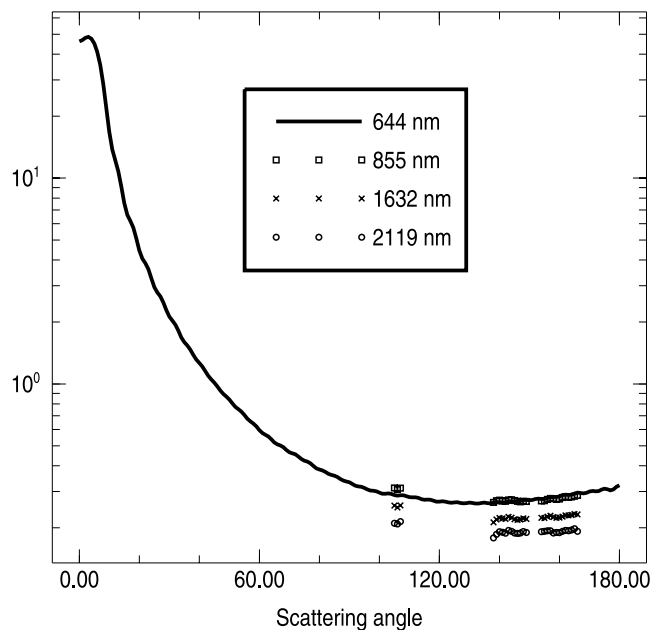
Figure 13. Calculated phase function of the POLDER nonspherical aerosol model, for different wavelengths. The 644 nm phase function [*Volten et al.*, 2001] is normalized but the forward peak is truncated. For other wavelengths, as we are using measurements realized from space, forward direction geometries are not available. For available scattering angles, tests described in section 7 discard a lot of coincidences. For a given scattering angle, if several coincidences are remaining after the tests, we have plotted the average value of the phase function.

nonspherical model from 670 to 865 nm. For middle-infrared wavelengths, Figure 13 shows significant shifts of the phase function. We compared, qualitatively, our results to computations of phase functions using the spheroid code of *Dubovik et al.* [2002b], for the same wavelengths as in Figure 13 (see Figure 14). The computation was done for feldspar, which is one of the samples used by *Volten et al.* [2001] in their averaged nonspherical scattering matrix. The results are encouraging; we can observe the same trends in Figures 13 and 14, i.e., negligible variation between visible and near infrared, but larger shift from visible to middle-infrared. Note that the shift in backward scattering directions for higher wavelengths is similar in Figures 13 and 14. According to the spheroid code, the expected spectral variation of the extinction coefficient for feldspar (thus of δ_λ^{NS}) is negligible from 644 to 855 nm but larger from 644 to 1632 nm (diminution of about 10 %) or to 2119 nm (diminution of about 20%). With our method, this effect is included in the phase function variation.

[48] Our method is giving an estimation of the nonspherical phase function in the middle-infrared by using simultaneous measurements of POLDER and MODIS. It is a good reference point for further studies. Efforts are underway to simulate the POLDER nonspherical model by using spheroid assumptions. A successful effort would result in a better characterization of nonspherical particles by POLDER in the infrared but also in the visible. Indeed, mineral samples used in the work of *Volten et al.* [2001] have been collected on the ground and may not represent

correctly mineral aerosols suspended in the air. Moreover, the *Volten et al.* [2001] experiment cannot perform measurements near scattering angles of 0° and 180° and an estimation has to be made on the energy scattered in the forward peak.

8. Overall Conclusion

[49] In this study we have compared radiance measurements and aerosol retrievals from POLDER 2 and MODIS instruments on board ADEOS 2 and Terra spacecrafts, respectively. Coincidence tables have been developed in order to compare information performed by the two sensors for the same spatial and temporal events. We have first compared geophysical products of both inversions (1): aerosol optical thickness at 865 nm, Angström exponent and small mode fraction at 865 nm. Then, we have simulated MODIS radiance measurements by using POLDER aerosol products (2) and inversely: starting from MODIS aerosol products, we have simulated POLDER total and polarized radiance measurements (3). The conclusions that we can make from these three points, presented below, will guide us in the construction of a coupled inversion which would make the best use of POLDER 2 and MODIS simultaneous measurements.

[50] 1. If we consider all coincidences, there is a general agreement between POLDER and MODIS results but large differences may occur. These differences are likely to be linked to particle shape effects. For cases where spherical particles dominate, results (aerosol optical thickness, Angström exponent, and fine mode fraction) of both inversions are comparable, especially for small aerosols. By contrast, when POLDER inversion indicates nonspherical particles, the MODIS inability to detect nonspherical aerosols leads to lower agreement with POLDER.

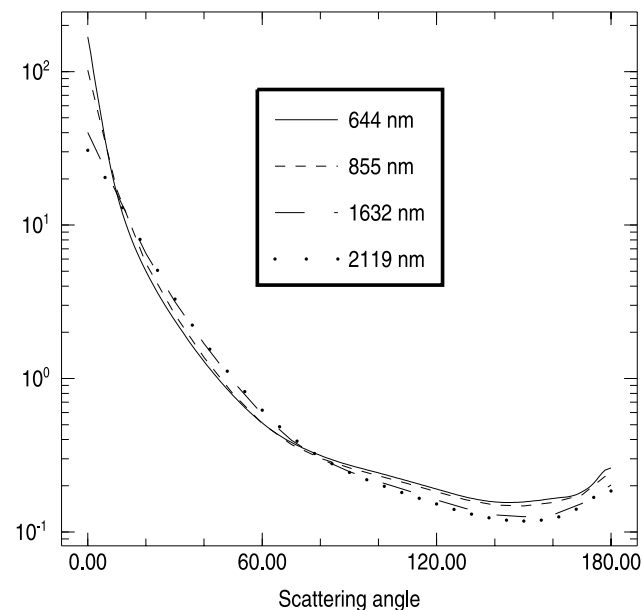[51] 2. Simulations using POLDER aerosol retrievals agree with the MODIS measurements for wavelengths near

Figure 14. Feldspar phase function, for different wavelengths, computed thanks to the spheroid code of *Dubovik et al.* [2002b].

POLDER ones. However, for middle-infrared channels, a systematic bias appears, especially in the case of nonspherical particles. This bias indicates that the optical properties of the nonspherical model used by POLDER exhibit clear spectral variations from the visible to the middle-infrared wavelengths. From POLDER and MODIS simultaneous measurements, we have obtained information on the nonspherical phase function behavior in the middle-infrared that can be used to constrain further studies.

[52] 3. Simulations of POLDER measurements by using MODIS aerosol products show a good retrieval of angularly averaged POLDER total or polarized measurements. However, they are not accurate enough to predict correctly directional behaviors for total and polarized light, especially for larger particles (spherical or not). The conclusion is that information provided by POLDER is particularly relevant to constrain the characterization of aerosol models (parameters of the size distribution, refractive index, and shape of large particles).

Appendix A: Acronyms

ADEOS	Advanced Earth Observing Satellite
AERONET	Aerosol Robotic Network
EOS	Earth Observing System
GLI	Global Imager
LANDSAT	Land Satellite
MISR	Multiangle Imaging Spectroradiometer
MODIS	Moderate Resolution Imaging Spectrometer
PARASOL	Polarization and Anisotropy of Reflectance for Atmospheric Sciences coupled with Observation from a Lidar
POLDER	Polarization and Directionality of Earth's Reflectance

Appendix B: Web Sites

ADEOS 2	ttp://sharaku.eorc.nasda.go.jp/ADEOS2/index.html
AERONET	http://aeronet.gsfc.nasa.gov/
AQUA	http://eos-pm.gsfc.nasa.gov/
ICARE	http://www-icare.univ-lille1.fr/icare/main.php
LOA	http://www-loa.univ-lille1.fr/
MISR	http://www-misr.jpl.nasa.gov/
MODIS	http://modis.gsfc.nasa.gov/about/index.html
POLDER	http://earth-sciences.cnes.fr/POLDER/
TERRA	http://terra.nasa.gov/
TOMS	http://jwocky.gsfc.nasa.gov/
Light Scattering Database	http://www.astro.uva.nl/scatter/

References

Ahmad, Z., and R. S. Fraser (1982), An iterative radiative transfer code for ocean-atmosphere system, *J. Atmos. Sci.*, *39*, 656−665.

Deschamps, P. Y., F. M. Bréon, M. Leroy, A. Podaire, A. Bricaud, J. C. Buriez, and G. Sèze (1994), The POLDER mission: Instrument characteristics and scientific objectives, *IEEE Trans. Geosci. Remote Sens.*, *32*, 598−615.

Deuzé, J. L., M. Herman, and R. Santer (1988), Fourier series expansion of the transfer equation in the atmosphere-ocean system, *J. Quant. Spectrosc. Radiat. Transfer*, *41*, 483−494.

Deuzé, J. L., P. Goloub, M. Herman, A. Marchand, G. Perry, S. Susana, and D. Tanré (2000), Estimate of the aerosol properties over the ocean with POLDER, *J. Geophys. Res.*, *105*, 15,329−15,346.

Deuzé, J. L., et al. (2001), Remote sensing of aerosols over land surfaces from POLDER-ADEOS-1 polarized measurements, *J. Geophys. Res.*, *106*, 4913−4926.

Diner, D. J., et al. (1998), Multi-angle Imaging SpectroRadiometer (MISR) description and experiment overview, *IEEE Trans. Geosci. Rem. Sens.*, *36*, 1072−1087.

Dubovik, O., B. N. Holben, T. F. Eck, A. Smirnov, Y. J. Kaufman, M. D. King, D. Tanré, and I. Slutsker (2002a), Variability of absorption and optical properties of key aerosol types observed in worldwide locations, *J. Atmos. Sci.*, *59*, 590−608.

Dubovik, O., B. N. Holben, T. Lapyonok, A. Sinyuk, M. I. Mishchenko, P. Yang, and I. Slutsker (2002b), Nonspherical aerosol retrieval method employing light scattering by spheroids, *Geophys. Res. Lett.*, *29*(10), 1415, doi:10.1029/2001GL014506.

Herman, M., J. L. Deuzé, A. Marchand, B. Roger, and P. Lallart (2005), Aerosol remote sensing from POLDER/ADEOS over the ocean. Improved retrieval using non-spherical particle model, *J. Geophys. Res.*, *110*, D10S02, doi:10.1029/2004JD004798.

Kaufman, Y. J., D. Tanré, L. A. Remer, E. F. Vermote, A. Chu, and B. N. Holben (1997), Operational remote sensing of tropospheric aerosol over land from EOS moderate resolution imaging spectroradiometer, *J. Geophys. Res.*, *102*, 17,051−17,067.

Kaufman, Y. J., D. Tanré, and O. Boucher (2002), A satellite view of aerosols in the climate system, *Nature*, *419*, 215−223.

King, M. D., Y. J. Kaufman, W. P. Menzel, and D. Tanré (1992), Remote sensing of cloud, aerosol, and water vapor properties from the Moderate Resolution Imaging Spectrometer (MODIS), *IEEE Trans. Geosci. Remote Sens.*, *30*, 2−27.

Levy, R. C., L. A. Remer, D. Tanré, Y. J. Kaufman, C. Ichoku, B. N. Holben, J. M. Livingston, P. B. Russel, and H. Maring (2003), Evaluation of the Moderate-Resolution Imaging Spectroradiometer (MODIS) retrievals of dust aerosol over the ocean during PRIDE, *J. Geophys. Res.*, *108*(D19), 8594, doi:10.1029/2002JD002460.

Martonchik, J. V., D. J. Diner, R. Kahn, T. P. Ackerman, M. M. Verstraete, B. Pinty, and H. R. Gordon (1998), Techniques for the retrieval of aerosol properties over land and ocean using multi-angle imaging, *IEEE Trans. Geosci. Rem. Sens.*, *36*, 1212−1227.

Mishchenko, M. I., and L. D. Travis (1997), Satellite retrieval of aerosol properties over the ocean using polarization as well as intensity of reflected sunlight, *J. Geophys. Res.*, *102*, 16,989−17,013.

Myhre, G., et al. (2004), Intercomparison of satellite retrieved aerosol optical depth over the ocean, *J. Atmos. Sci.*, *61*, 499−513.

Ramanathan, V., P. J. Crutzen, J. T. Kiehl, and D. Rosenfeld (2001), Aerosols, climate, and the hydrological cycle, *Science*, *294*(5549), 2119−2124.

Remer, L. A., et al. (2005), The MODIS aerosol algorithm, products and validation, *J. Atmos. Sci.*, *62*, 947−973.

Salomonson, V. V., W. L. Barnes, P. W. Maymon, H. E. Montgomery, and H. Ostrow (1989), MODIS: Advanced facility instrument for studies of the Earth as a system, *IEEE Trans. Geosci. Remote Sens.*, *27*, 145−153.

Tanré, D., Y. J. Kaufman, M. Herman, and S. Mattoo (1997), Remote sensing of aerosol properties over oceans using the MODIS/EOS spectral radiances, *J. Geophys. Res.*, *102*, 16,971−16,988.

Volten, H., O. Muñoz, E. Rol, J. F. de Haan, W. Vassen, J. W. Hovenier, K. Muinonen, and T. Nousiainen (2001), Scattering matrices of mineral aerosol particles at 441.6 nm and 632.8 nm, *J. Geophys. Res.*, *106*, 17,375−17,401.

Wang, M., and H. R. Gordon (1994), Radiance reflected from the ocean-atmosphere system: Synthesis from individual components of the aerosols size distribution, *Appl. Opt.*, *33*, 7088−7095.

───────────

J.-L. Deuzé, B. Gérard, M. Herman, P. Lallart, C. Oudard, and D. Tanré, Laboratoire d'Optique Atmosphérique, Université des Sciences et Technologies de Lille, Villeneuve d'Ascq, F-59655, France. (benoit.gerard@loa.univ-lille1.fr)

Y. J. Kaufman and L. A. Remer, Laboratory for Atmospheres, NASA Goddard Space Flight Center, Greenbelt, MD 20771, USA.

B. Roger, Pôle ICARE, Université des Sciences et Technologies de Lille, Villeneuve d'Ascq, F-59655, France.

B. Six, Centre de Ressources Informatiques, Université des Sciences et Technologies de Lille, Villeneuve d'Ascq, F-59655, France.